PERGAMON

International Journal of Heat and Mass Transfer 45 (2002) 609–618

International Journal of HEAT and MASS TRANSFER

www.elsevier.com/locate/ijhmt

Experimental and numerical study on a miniature Joule–Thomson cooler for steady-state characteristics

K.C. Ng [a], H. Xue [b,*], J.B. Wang [a]

[a] *Department of Mechanical Engineering, National University of Singapore, 119260 Singapore, Singapore*

[b] *Mechanical Engineering Department, California State Polytechnic University, 3801 West Temple Avenue, Pomona, CA 91768, USA*

Received 22 January 2001; received in revised form 14 April 2001

Abstract

A miniature Joule–Thomson (JT) cooler with a recuperative heat exchanger is studied, both theoretically and experimentally, for its steady-state behaviors down to 96 K. Two unique aspects of analysis are presented in this paper. Firstly, the simulation employs a distributed approach (as opposed to a black-box) and it is performed with dynamic updating of the thermo-physical properties of the working fluid when the governing differential equations are solved simultaneously. Secondly, the conduction heat leak effects in the longitudinal direction of the exchanger are included along with those from the ambient. The properties of Argon, expressed as a function of the local values of P and T, have been found to compare well with data obtained from tables of IUPAC. Our experiments on the JT cooler indicate good agreement with the predictions to within a relative error of $\pm 0.3\%$ across a large span of Argon pressures.

Keywords: JT cooler; Experimental and numerical study; Steady-state characteristics; Temperature-dependent properties; Longitudinal heat conduction

1. Introduction

The Joule–Thomson (JT) cooler is one of the most effective methods of providing low-temperature cooling of electronic components such as IR detectors, SQUID and CMOS-IC chips. This is because of its special features of short cool-down time, simple miniaturized dimensions and no moving parts. The cooling power is generated by the isenthalpic expansion of a high-pressure gas through a throttling (capillary) device or simply known as the JT effect. The performance of the JT cooler can be amplified by using the recuperative effect of the expanded gas to pre-cool the incoming stream within a counter-flow exchanger.

There has been a plethora of articles focusing on the fabricating JT cooler using different structure and materials. The majority of miniature heat exchanger design follows either (i) the Hampson-type or (ii) the Linde-type exchanger. The latter exchanger design is more traditional and it is usually made from concentric or solder-boned parallel tubes. The former design is widely used both in conventional and miniature designs. The high-pressure tube in the Hampson exchanger is finned with copper ribbon and they are usually wound in a helical annular space between two co-axial cylinders [1,2]. Recent developments of JT cooler have been in the realm of miniaturization of the heat exchanger using photolithographic technique and others. It allows the fabrication of planar exchanger or known commonly as micro-miniature refrigerator (MMR). Such MMR technologies can produce coolers up to 500 mW using Argon at a low temperature of 90 K [3,4]. Another type of JT cooler uses a heat exchanger made from sintered metal powder. It operates with a cooling power of 1700 mW with only 10 MPa Argon [5–7].

Numerical studies on the JT cooler have also been reported with special focus on the cool-down rates [8–14]. Many of these theoretical analyses could have been ignored with distributed modeling and their models are

* Corresponding author. Tel.: +1-909-869-4304; fax: +1-909-869-4341.

E-mail address: hxue@csupomona.edu (H. Xue).

0017-9310/02/$ - see front matter
PII: S0017-9310(01)00165-X

Nomenclature

A	cross-sectional area of flow passage, m^2
C_p	isobaric specific heat, J/(kg K)
C_v	isochoric specific heat, J/(kg K)
D, d	diameter of tubes, m
dx	grid length along x coordinate, m
f	Fanning friction factor
G	mass velocity, kg/(m^2 s)
h	heat transfer coefficient, W/(m^2 K)
L	length of the heat exchanger, m
k	thermal conductivity, W/(m K)
$\dot{m}$	mass flow rate, kg/s
M_v	volumetric flow rate, SLPM
P	pressure, Pa
p	perimeter of heat transfer, m
Pr	Prandtl number
R	ideal gas constant, J/(kg K)
Re	Reynolds number
T	temperature, K
u	gas average velocity, m/s
x	axial coordinate, m
$f\{T,P\}$	f as a function of T and P

Greek symbols

λ	thermal conductivity, W/(m K)
η	dynamic viscosity, Pa s
σ	Stefan–Boltzmann constant
ρ	density, kg/m^3

Subscripts

amb	ambient (room temperature) condition
c	cold fluid or low-pressure gas
ci	capillary inside
co	capillary outside
cr	critical state
cu	copper
H	hydraulic
h	hot fluid or high-pressure gas
hel	helical
in	inlet
m	mandrel
mo	mandrel outside
mn	monel alloy
out	outlet
pc	polycarbonate
r	radiation
s	shield
si	shield inside
so	shield outside
ss	stainless steel
w	wall of finned capillary

seldom validated with measured data. Some analyses ignored the presence of heat leak from the longitudinal direction of the heat exchanger. It is our objective in this paper to address both issues of distributed analysis and experimental verification.

2. Theoretical model

A schematic of the Hampson-type counter-flow heat exchanger is shown in Fig. 1. The characteristic size of the JT cooler used in experiments is tabulated in Table 1. Consider an element of the heat exchanger, the high-pressure gas flows inside the coiled-capillary whilst the low-pressure gas flows on the outside but in opposite direction. The control volume to be modeled comprises the two mentioned gas streams as well as the thermal capacities of the coils, a mandrel and an external shield. Heat conduction in the radial and the longitudinal directions are also incorporated in the model where their heat rates can affect the local properties of fluid. To acquire more accurate results, the thermo-physical properties of fluids are integrally solved with the governing system of differential equations. The equation Jacobians with respect to temperature and pressure are also simultaneously updated. The minimum 'free-flow' area approach [15] is used to determine the local Reynolds number and convective heat transfer coefficients. All characteristic dimensions are based on the hydraulic diameter (D_H) concept. We will now describe the sets of governing equations in the sections below.

2.1. Continuity equation

For one-dimensional steady-state flow, the mass flow rate is governed by continuity equation

$$\frac{d\dot{m}}{dx} = \frac{d(GA)}{dx} = 0, \tag{1}$$

where $\dot{m} = \rho u A = GA$ is a constant, G is the mass velocity of fluid and volume flow rate is given by $M_v = \dot{m}/\rho$.

2.2. Momentum equation

Owing to the high pressure drop in the exchanger (caused by high flow velocity in the helical capillary), the friction factor (f), density (ρ) and the local average velocity (u) are all dependent on the local T and P of working fluid. From the Navier–Stokes equations, it can be easily shown that pressure drop along the longitudinal direction of the capillary is given by

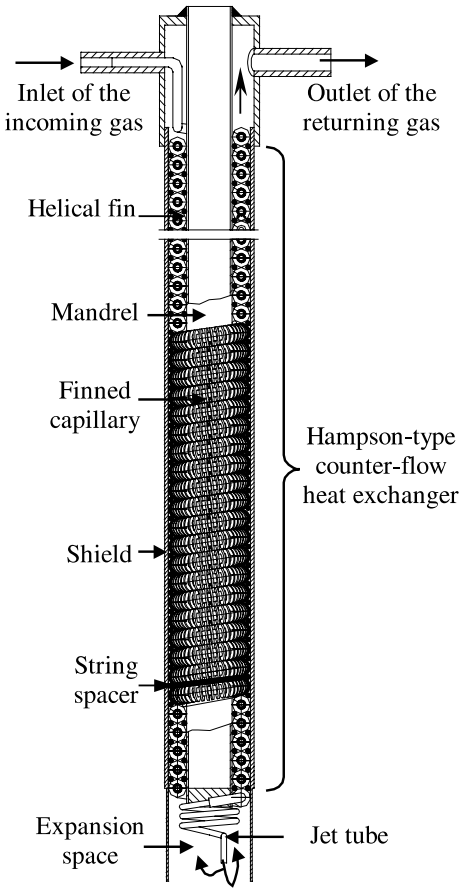

Fig. 1. Hampson-type JT cooler.

Table 1
The characteristic sizes of the JT cooler used in experiments

The inside diameter of the capillary, d_{ci}	0.3 mm
The outside diameter of the capillary, d_{co}	0.5 mm
The inside diameter of the mandrel, d_{mi}	2.3 mm
The outside diameter of the mandrel, d_{mo}	2.5 mm
The inside diameter of the mandrel, d_{si}	4.5 mm
The outside diameter of the shield, d_{so}	4.8 mm
The length of the recuperative heat exchanger, L	50 mm

$$\frac{\mathrm{d}p}{\mathrm{d}x}=\left(\frac{2f\{P,T\}}{\rho\{P,T\}D_{\mathrm{H}}}\right)\Big/\left(\frac{\mathrm{d}\rho\{P,T\}/\mathrm{d}P}{\rho^2\{P,T\}}-\frac{1}{G^2}\right), \tag{2}$$

where $\mathrm{d}\rho\{P,T\}/\mathrm{d}P$ is given by the equation of state of working gas, Argon. It is noted that the Fanning friction factor expression for flow in a helical coil is given by [16,22]

$$f\{P,T\}=0.184(1+3.5D_{\mathrm{ci}}/D_{\mathrm{hel}})/Re^{0.2}\{P,T\}. \tag{3}$$

2.3. Energy equations

Energy conservation for the control volume can be derived separately for the following components of the exchanger. (The symbols used have their usual meanings, as outlined in the nomenclature.)

(i) *High pressure gas side*:

$$\dot{m}_{\mathrm{h}}Cp_{\mathrm{h}}\{P_{\mathrm{h}},T_{\mathrm{h}}\}\frac{\mathrm{d}T_{\mathrm{h}}}{\mathrm{d}x}=h_{\mathrm{h}}\{P_{\mathrm{h}},T_{\mathrm{h}}\}p_{\mathrm{ci}}(T_{\mathrm{w}}-T_{\mathrm{h}}). \tag{4}$$

(ii) *Low pressure fluid side*:

$$\dot{m}_{\mathrm{c}}Cp_{\mathrm{c}}\{P_{\mathrm{c}},T_{\mathrm{c}}\}\frac{\mathrm{d}T_{\mathrm{c}}}{\mathrm{d}x}=h_{\mathrm{c}}\{P_{\mathrm{c}},T_{\mathrm{c}}\}[p_{\mathrm{co}}(T_{\mathrm{c}}-T_{\mathrm{w}})+p_{\mathrm{si}}(T_{\mathrm{c}}-T_{\mathrm{s}})+p_{\mathrm{mo}}(T_{\mathrm{c}}-T_{\mathrm{m}})]. \tag{5}$$

(iii) *Finned capillary*:

$$k_{\mathrm{w}}\{T_{\mathrm{w}}\}A_{\mathrm{w}}\frac{\mathrm{d}^2T_{\mathrm{w}}}{\mathrm{d}x^2}=h_{\mathrm{h}}\{P_{\mathrm{h}},T_{\mathrm{h}}\}p_{\mathrm{ci}}(T_{\mathrm{w}}-T_{\mathrm{h}})+h_{\mathrm{c}}\{P_{\mathrm{c}},T_{\mathrm{c}}\}p_{\mathrm{co}}(T_{\mathrm{w}}-T_{\mathrm{c}}). \tag{6}$$

(iv) *Mandrel tube*:

$$k_{\mathrm{m}}\{T_{\mathrm{m}}\}A_{\mathrm{m}}\frac{\mathrm{d}^2T_{\mathrm{m}}}{\mathrm{d}x^2}=h_{\mathrm{c}}\{P_{\mathrm{c}},T_{\mathrm{c}}\}p_{\mathrm{mo}}(T_{\mathrm{m}}-T_{\mathrm{c}}). \tag{7}$$

(v) *Shield tube*:

$$k_{\mathrm{s}}\{T_{\mathrm{s}}\}A_{\mathrm{s}}\frac{\mathrm{d}^2T_{\mathrm{s}}}{\mathrm{d}x^2}=h_{\mathrm{c}}\{P_{\mathrm{c}},T_{\mathrm{c}}\}p_{\mathrm{si}}(T_{\mathrm{s}}-T_{\mathrm{c}})+h_{\mathrm{r}}\{T_{\mathrm{s}}\}p_{\mathrm{so}}\left(T_{\mathrm{s}}^4-T_{\mathrm{amb}}^4\right). \tag{8}$$

Radiative effect between the ambient and the shield is accounted for in the energy balance of our model. The radiative factor of heat exchanger is given by

$$h_{\mathrm{r}}\{T_{\mathrm{s}},T_{\mathrm{amb}}\}=\sigma\Big/\left[\frac{1}{e_{\mathrm{s}}\{T_{\mathrm{s}}\}}+\frac{A_{\mathrm{so}}}{A_{\mathrm{r}}}\left(\frac{1}{e_{\mathrm{r}}\{T_{\mathrm{amb}}\}}-1\right)\right], \tag{9}$$

where e_{s} and e_{r} are emissivities of the shield and ambient, respectively.

A well-known turbulent flow correlation for convective heat transfer coefficient, as proposed by Flynn [16], is employed in the modeling, i.e.,

$$h_{\mathrm{h}}\{P_{\mathrm{h}},T_{\mathrm{h}}\}=0.023Cp_{\mathrm{h}}\{P_{\mathrm{h}},T_{\mathrm{h}}\}G_{\mathrm{h}}Re_{\mathrm{h}}^{-0.2}\{P_{\mathrm{h}},T_{\mathrm{h}}\}Pr_{\mathrm{h}}^{-2/3}\times\{P_{\mathrm{h}},T_{\mathrm{h}}\}(1+3.5D_{\mathrm{ci}}/D_{\mathrm{hel}}), \tag{10}$$

where $G_{\mathrm{h}}=\dot{m}/A_{\mathrm{h}}$. For the convective heat transfer coefficients of returning cold fluid (denoted by the subscript c) in the JT exchanger, the empirical correlation suggested by Flynn [16] is used

$$h_{\mathrm{c}}\{P_{\mathrm{c}},T_{\mathrm{c}}\}=0.26Cp_{\mathrm{c}}\{P_{\mathrm{c}},T_{\mathrm{c}}\}G_{\mathrm{c}}Re_{\mathrm{c}}^{-0.4}\{P_{\mathrm{c}},T_{\mathrm{c}}\}Pr_{\mathrm{c}}^{-2/3}\{P_{\mathrm{c}},T_{\mathrm{c}}\}, \tag{11}$$

where $G_c = \dot{m}/A_c$, and the above correlation is suitable for the range of turbulent flow of $2 \times 10^3 < Re < 3.2 \times 10^4$. An equivalent hydraulic diameter ($D_{H,c}$) is used for calculating the Reynolds number.

It is noted that Eqs. (2)–(11) are all dependent on P and T of working gas along each section of the exchanger. Owing to the coupled nature of differential equations on the properties of the working gas, namely Argon, the following section is devoted to describing how the salient properties of Argon vary during depressurization through the exchanger.

2.4. Thermo-physical properties of Argon

In this section, a brief description of the correlations, used to obtain the thermo-physical properties of Argon, will be discussed. The relationship for computing P as a function T and ρ is based on the modified Benedict–Webb–Rubin (MBWR) equation of state which has 32 coefficients [17]. This equation provides the versatility and adaptability for physical property simulation of Argon, and it employs the multi-property fitting technique where deviations from the experimental data (*PVT* surface and density) are minimized. Hence, the advantages of MBWR are its accurate representation of *PVT* surface and convenience in correlating real experimental data of different sources. For the sake of completeness, we present the algebraic equations for four salient properties used in our computer program, namely the density, specific heat, viscosity and thermal conductivity.

The equation of state, expressed here in terms of P in the mathematical form of the MBWR, is given as follows:

$$\begin{aligned} P = {} & \rho RT + \rho^2\left(G_1T + G_2T^{1/2} + G_3 + G_4/T + G_5/T^2\right) \\ & + \rho^3\left(G_6T + G_7 + G_8/T + G_9/T^2\right) \\ & + \rho^4(G_{10}T + G_{11} + G_{12}/T) + \rho^5G_{13} \\ & + \rho^6\left(G_{14}/T + G_{15}/T^2\right) + \rho^7(G_{16}/T) \\ & + \rho^8\left(G_{17}/T + G_{18}/T^2\right) + \rho^9\left(G_{19}/T^2\right) \\ & + \rho^3\left(G_{20}/T^2 + G_{21}/T^3\right)\exp\left(\gamma\rho^2\right) \\ & + \rho^5\left(G_{22}/T^2 + G_{23}/T^4\right)\exp\left(\gamma\rho^2\right) \\ & + \rho^7\left(G_{24}/T^2 + G_{25}/T^3\right)\exp\left(\gamma\rho^2\right) \\ & + \rho^9\left(G_{26}/T^2 + G_{27}/T^4\right)\exp\left(\gamma\rho^2\right) \\ & + \rho^{11}\left(G_{28}/T^2 + G_{29}/T^3\right)\exp\left(\gamma\rho^2\right) \\ & + \rho^{13}\left(G_{30}/T^2 + G_{31}/T^3 + G_{32}/T^4\right)\exp\left(\gamma\rho^2\right), \end{aligned} \quad (12)$$

where the non-linear coefficient $\gamma = -1/\rho_{cr}^2$ is assumed constant, G_i are linear coefficients and their values are available from Refs. [17,18]. Given an inlet measurement of P in the test facility, the corresponding density of Argon at a local P and T can be determined by solving the above-mentioned non-linear MBWR equation. Fig. 2 shows the variation of density at values of T from 90 to 300 K and P from 0.1 to 20 MPa. The collation of the density lines at high pressure ($P > 6$ MPa) and low temperature ($T < 120$ K) indicates that the Argon gas is at the super-compressed state. At higher temperatures ($T > 180$ K), the density of Argon decreases in a uniform manner. Significant change in density of Argon is expected at conditions near its critical point region ($P_{cr} = 4.862$ MPa, $T_{cr} = 150.73$ K).

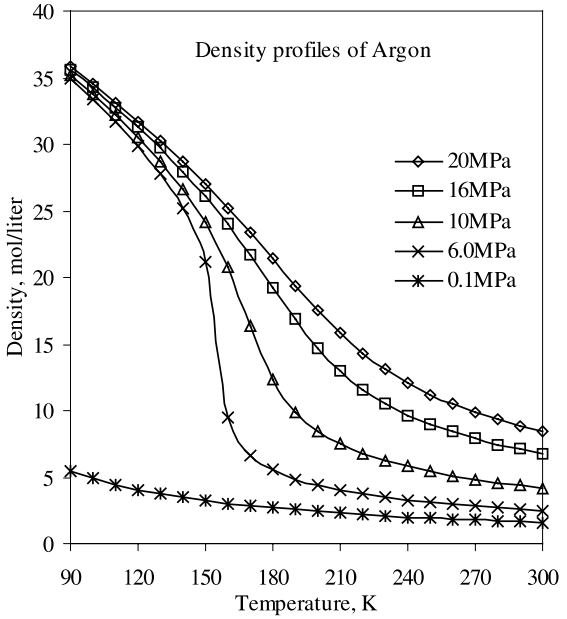

Fig. 2. Variation of density of Argon.

The specific heat of Argon is also a function of temperature and density and it is given by

$$C_p\{T,\rho\} = C_v\{T,\rho\} + \left[\frac{T}{\rho^2}\left(\frac{\partial P}{\partial T}\right)_\rho^2 \Big/ \left(\frac{\partial P}{\partial \rho}\right)_T\right], \quad (13)$$

where $C_v\{T,\rho\}$ is the isochoric specific heat of the form

$$C_v\{T,\rho\} = \left(C_p^0\{T\} - R\right) - \int_0^\rho \left[T/\rho^2\left(\partial^2 P/\partial T^2\right)_\rho\right]_T \mathrm{d}\rho, \quad (14)$$

where $C_p^0\{T\}$ is the specific heat of Argon in ideal gas state, it can be calculated by

$$C_p^0\{T\} = R\left[\sum_{i=1}^{9}\left(N_iT^{i-4}\right) + N_8u^2e^u \Big/ \left(e^u - 1\right)^2\right], \quad (15)$$

where $u = N_9/T$ and $N_1, N_2, N_3, \ldots, N_9$ are the coefficients for the ideal behavior of Argon [17]. Fig. 3 shows the P and T-dependency of the specific heat of Argon. Close to its critical region, C_p tends to rise sharply towards a peak. This can be attributed to the non-suitability of correlation for a narrow region around the critical states [17].

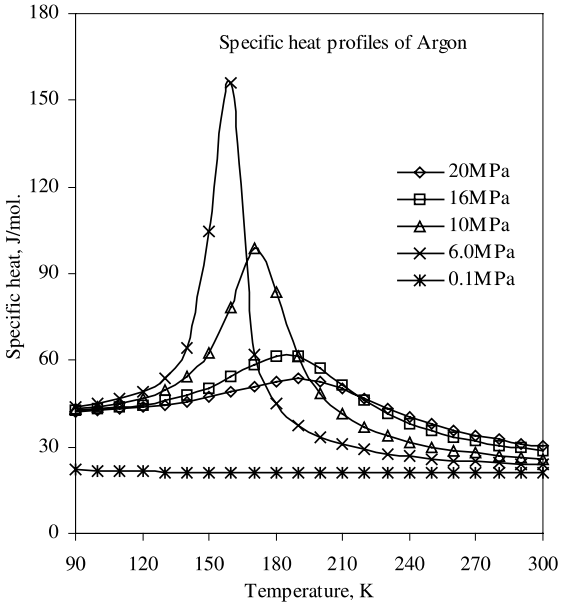

Fig. 3. Temperature and pressure-dependent specific heat of Argon.

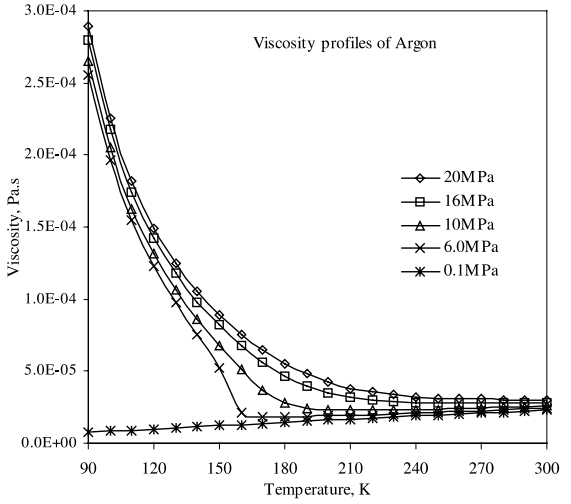

Fig. 4. Temperature and pressure-dependent viscosity of Argon.

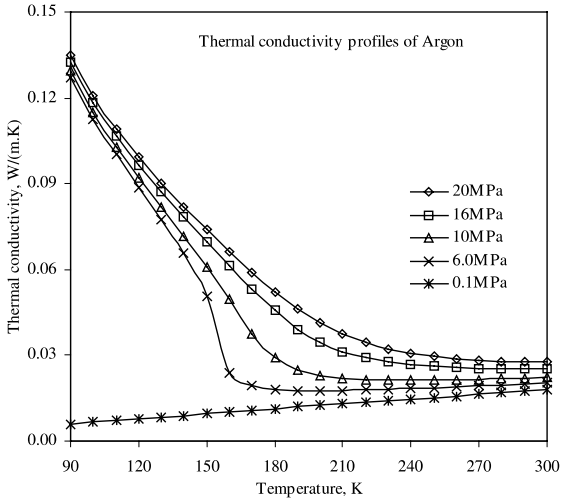

Fig. 5. Temperature and pressure-dependent thermal conductivity of Argon.

Similarly, the functional forms for viscosity and thermal conductivity are

$$\eta\{T,\rho\} = \eta_0\{T\} + \eta_1\{T\}\rho + \eta_2\{T,\rho\}, \tag{16}$$

and

$$\lambda\{T,\rho\} = \lambda_0\{T\} + \lambda_1\{T\}\rho + \lambda_2\{T,\rho\} + \lambda_{cr}\{T,\rho\}. \tag{17}$$

The first terms of Eqs. (16) and (17) are the contributions of dilute gas. Their second terms represent the contribution from transport coefficients of the moderately dense gas and the third terms are the contribution of dense gas behavior. The last term of thermal conductivity accounts for the critical enhancement effect. It is well established that the thermal conductivity coefficient increases sharply in the regions close to the critical point. All coefficients of the above expressions are given in Hanley's work [18]. The profiles of viscosity and thermal conductivity with respect to P and T are shown in Figs. 4 and 5, and their trends are similar. A comparison of thermo-physical properties from the correlations is compared with the tabulated data of International Thermodynamic Table [19] shows good agreement. The deviations in density, specific heat and viscosity all are less than 0.3%, and those of thermal conductivity are less than 0.5%, except a narrow temperature and pressure range near the critical point.

2.5. Thermal conductivities of JT exchanger materials

Temperature-dependent thermal conductivities of materials used in the fabrication of JT exchanger, such as copper (for the finned capillary), monel (for the mandrel) and stainless steel or polycarbonate (for the shield) are used in the simulation, and their relevant correlations are summarized in Table 2 [20,21].

We solve the governing differential equations using a finite-volume approach with judicious selection of grid sizes so as to increase the speed of convergence of solutions. A schematic of gas flows with the control-volume is shown in Fig. 6. During iterations, the dynamic state thermo-physical properties of Argon are updated according to the local values of P and T. The boundary conditions for the momentum and energy equations (2), (4)–(8) are as follows:

Table 2
Thermal conductivities of solid materials used in the JT cooler

Materials	Correlations	Errors
Copper	$k_{cu} = \begin{cases} 0.0028T^2 - 1.525T + 608 & (100\ \mathrm{K} \leqslant T \leqslant 300\ \mathrm{K}) \\ 0.2413T^2 - 47.775T + 2848 & (60\ \mathrm{K} \leqslant T \leqslant 100\ \mathrm{K}) \end{cases}$	Less than 1.5%
Monel alloy	$k_{mn} = 6.5169 \ln T - 14.76 \quad (40\ \mathrm{K} \leqslant T \leqslant 400\ \mathrm{K})$	Less than 1%
Stainless steel	$k_{ss} = 5.0353 \ln T - 13.797 \quad (40\ \mathrm{K} \leqslant T \leqslant 400\ \mathrm{K})$	Less than 1
Polycarbonate	$k_{pc} = 0.22 \quad (40\ \mathrm{K} \leqslant T \leqslant 400\ \mathrm{K})$	–

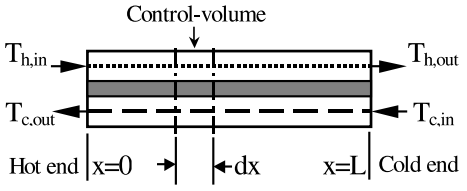

Fig. 6. Model of a counter flow heat exchanger.

$$\begin{aligned} &\text{At } x = 0, \quad T_h = T_{h,in}, \quad dT_w/dx = 0, \quad dT_s/dx = 0, \\ &\qquad dT_m/dx = 0, \quad P = P_{h,in}, \\ &\text{At } x = L, \quad T_c = T_{c,in}, \quad dT_w/dx = 0, \quad dT_s/dx = 0, \\ &\qquad dT_m/dx = 0. \end{aligned}$$

The assembled computer code invokes the IMSL routines, called DBVPFD. It is solved on a PC using a Fortran compiler with typical CPU time of 20 min per run. The number of iteration in such a run is about 500 iterations.

3. Experimental apparatus and procedures

Fig. 7 shows the overall arrangement of the JT cooler testing facility with detailed locations of P and T sensors. Argon gas of 99.9995% purity and 12–18 MPa is tapped from a gas tank into a tabular conduct of 1.6 mm diameter before entering the Hampson-type JT cooler. Within the recuperative heat exchanger, the high pressure Argon is expanded in the helical finned capillary tube where JT effect is produced by the rapidly expanding gas. At the end of the helical tube, Argon is further expanded at the "jet-tube" at sonic speeds, reaching the vapor–liquid states corresponding to its local P and T. Arbitrary heating is supplied to the impinging jet of Argon by an external DC heater which can be controlled during experiment up to 4.5 W. The recuperative action of the returning gas, which flows over the outside surface of the helical tubes, further cools the incoming high enthalpy gas and thus, amplifying the JT coefficient of the Argon gas in its expansion process.

We measure the temperatures and pressures at two ends of JT exchanger. Type K thermocouples that are mineral-insulated stainless steel sheathed probes are used for measuring temperature. The probe diameter is 0.5 mm. Thermocouples were calibrated with an accuracy of ±1°C. Three pressure transducers with fully signal conditioned and temperature compensated functions are utilized to record the pressure, which were calibrated with a relative accuracy of 1%. The mass flow rate is also measured. Flow rate sensor is a micro-bridge mass airflow with the linearity error of ±3% reading, and repeatability and hysteresis of ±0.5% reading. An experimental system comprising five major apparatus was designed and set up, as shown in Fig. 8. The sensors were connected to a HP 34970A data logger from which experimental data can be automatically recorded.

The experimental procedures are briefly described as follows:

(a) All components, units, systems and pipeline are assembled according to the design layout shown in Fig. 8, and check for zero leakage in all parts.
(b) Input the calibration data of sensors into the control computer then download the pre-set up data to the data logger. Conduct a self-testing of the automatic record system, prior to scanning of data.
(c) Adjust the inlet supply pressure ($P_{h,in}$) to the desired level using a gas regulator.
(d) The thermocouple at cold jet would record a gradual reduction in temperature. When the variation of this temperature is less than ±1 K, the JT cooler is regarded as operating on steady state.
(e) Keep the steady-state process until all data have been recorded by the data logger. Close the valve of gas cylinder.
(f) Repeat steps (c)–(e), to obtain the assorted experimental data at pre-selected pressures.

4. Results and discussion

In a given test, the following measurements are monitored for 180 s: $P_{h,in}$, $T_{h,in}$, $P_{c,in}$, $T_{c,in}$, M_v and $T_{c,out}$. Table 3 tabulates the experimental results of five assorted Argon gas inlet pressures, as well as a comparison between the predicted and measured $T_{c,out}$. As evidenced in the table, the relative errors are less than 0.3%. The temperature and pressure–time traces for two values of $P_{h,in}$, namely, 17.912 and 14.047 MPa, are shown in Figs. 9 and 10, respectively. For a given steady-state conditions, it is observed that the JT cooler has a rapid cold-

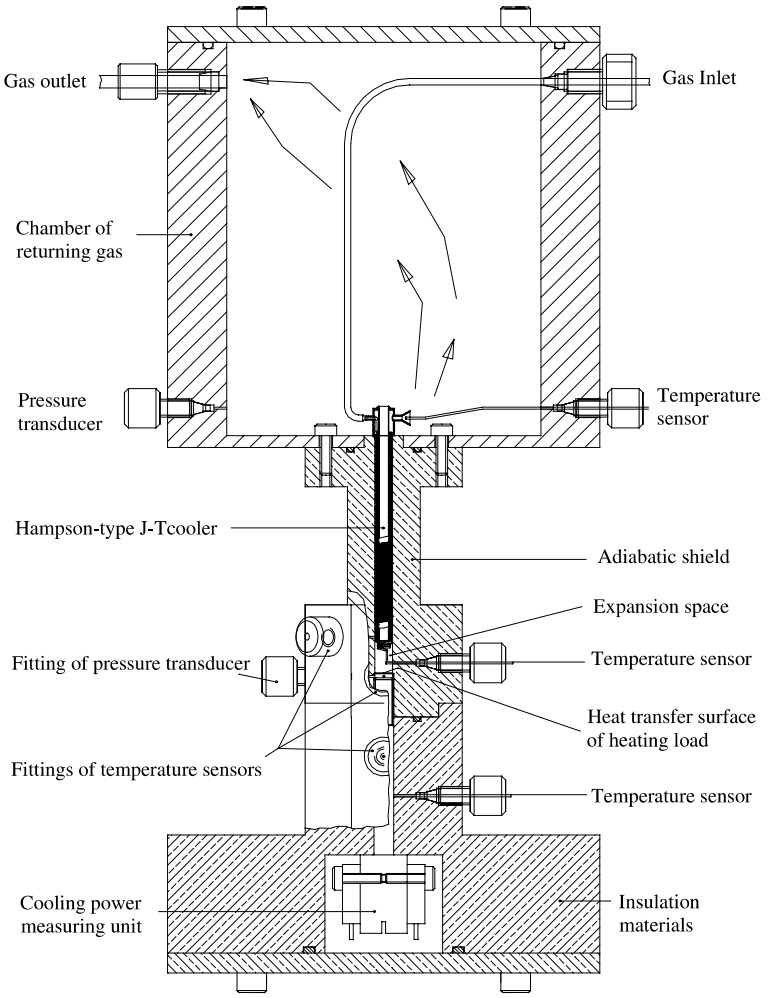

Fig. 7. JT cooler testing facility.

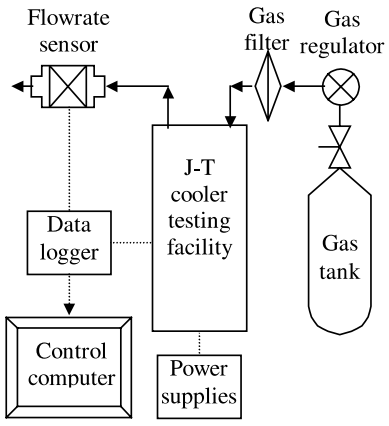

Fig. 8. Schematic of experimental apparatus.

down rate at higher supply pressure, typically about 50 s. As observed in Figs. 9 and 10, the starting inlet temperatures of the hot and cold streams are unequal because the tests were not started from "cold" conditions – meaning that there were tests made prior to these steady-state runs. The minimum temperature achieved at the cold end is around 96–110 K. Steady-state conditions are achieved in less than a minute after the commencement of gas flow for all tests. The time cut-off was 3 min to save Argon. The measured temperature and pressure uncertainties are ± 1.1 K and $\pm 1.5\%$, respectively, and the uncertainty for flow rate is $\pm 3.4\%$.

To conduct numerical predictions, five boundary conditions of the working fluid including inlet-temperatures and inlet-pressures at two ends of counter-flow heat exchanger and flow rate must be input into simulating program. The temperature distributions and pressure drop profile can be obtained by solving the set

Table 3
Experimental data and simulation results of $T_{c,out}$

$P_{h,in}$ (MPa)	$P_{c,in}$ (MPa)	M_v (SLPM)	$T_{h,in}$ (K)	$T_{c,in}$ (K)	$T_{c,out}$ (K)		
					Experiment	Simulation	Relative error (%)
17.912	0.17272	13.927	291.49	110.36	282.57	282.85	0.0995
16.986	0.17460	13.102	291.40	110.42	283.73	282.90	−0.292
16.010	0.16362	11.943	292.25	109.90	284.77	284.07	−0.246
14.966	0.14713	10.948	292.14	109.28	284.90	284.19	−0.248
14.047	0.13426	10.145	291.94	108.70	284.98	284.15	−0.293

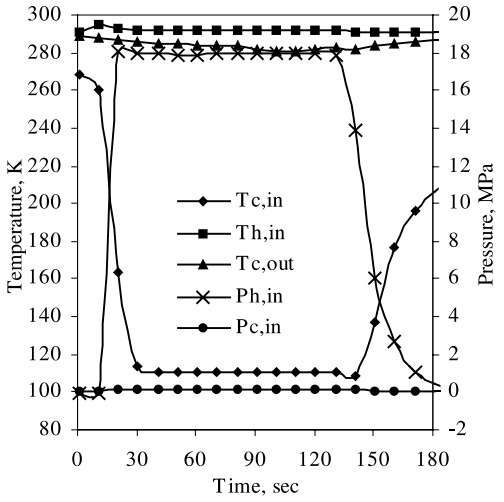

Fig. 9. Temperature and pressure-time history of the JT cooler at $P_{h,in} = 17.912$ MPa. The external heating load is 17.83 W/cm^2.

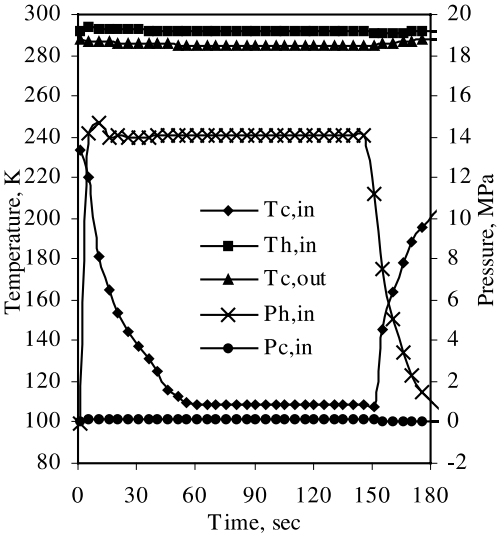

Fig. 10. Temperature and pressure-time history of the JT cooler at $P_{h,in} = 14.047$ MPa. The external heating load is 17.83 W/cm^2.

of governing equations outlined in Section 2. The steady-state temperature distributions of incoming gas, returning gas, finned capillary, mandrel and shield are shown in Fig. 11 and 12 for two cases of incoming pressure gas, $P_{h,in} = 17.912$ and 14.047 MPa, respectively.

Experimental verification of the simulation code is conducted by measuring the temperature at the hot end of JT exchanger. It is observed that there is good agreement between predication results and experimental data, and the change of inlet pressure of incoming gas has insignificant effect on this temperature. This is attributed to high effectiveness of JT exchanger and the attainment of vapor liquid in the cold end of the JT cooler.

It is noted that although the externally supplied power is 4.5 W, the net cooling power seen at the cold end is only 3.5 W, due mainly to the heat losses along the stem of the heater. This rate of cooling would correspond to a cooling density of 18 W/cm^2 at cold end temperature of 90–110 K. This amount of cooling density is twice of the present generation of commercial IC chips, such as high performance CPU, DRAM, etc. [23].

5. Conclusions

We have successfully modeled the miniature JT cooler using a fully distributed simulation where the thermo-fluids properties of the expanding gas, namely Argon, are tracked, updated and solved along with the governing equations. Our distributed modeling technique gives excellent agreement between the experimental data and numerical computation. This is because the model captures the main physics of the JT effect of the expanding Argon.

The simulation code is validated by experiments on a specially designed JT cooler of nominally 3.5 W cooling capacity or about 18 W/cm^2. The experimental and predicted results are depicted on non-dimensional plots. The lowest temperature of jet orifice was measured at 96 K whilst the cold-chamber temperature during steady state achieved approximately 110 K. It is found that the cooling density produced by the JT cooler is twice that of the present heat release density of today's IC chips.

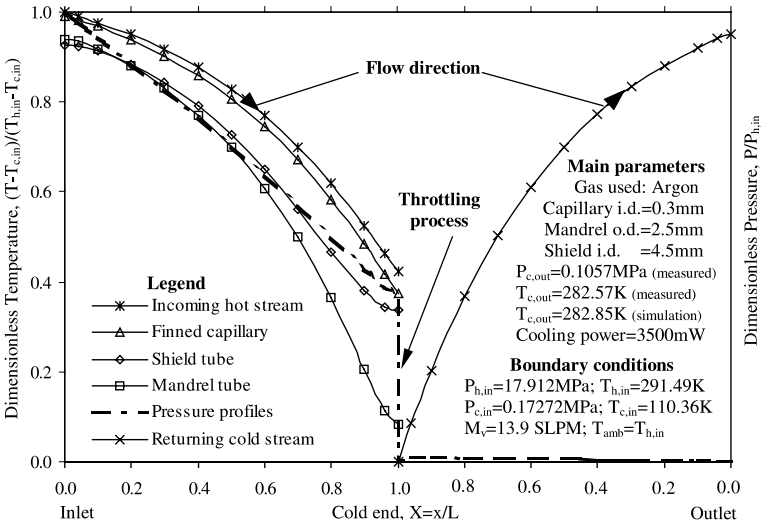

Fig. 11. Steady-state temperature and pressure profiles of the JT cooler at $P_{h,in} = 17.912$ MPa, $M_v = 13.927$ SLPM.

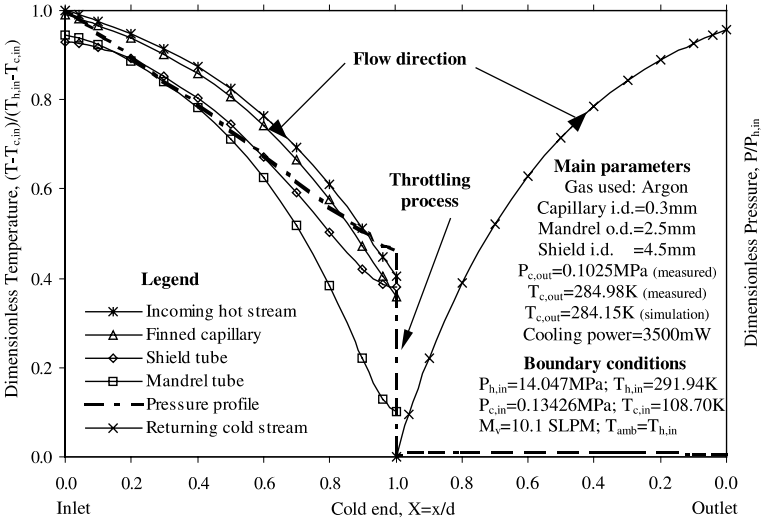

Fig. 12. Steady-state temperature and pressure profiles of the JT cooler at $P_{h,in} = 14.047$ MPa, $M_v = 10.145$ SLPM.

In addition to steady-state characteristics, the experimental results also show realistic initial pull down behaviors and these information are useful for improving the design of JT mini-cooler.

References

[1] G.K. White, in: Experimental Techniques in Low-Temperature Physics, Clarendon Press, Oxford, 1987, pp. 59–73.
[2] R.F. Barron, Cryogenic Heat Transfer, Taylor & Francis, London, 1999.
[3] W.A. Little, Micro miniature refrigeration, Rev. Sci. Instr. 55 (5) (1984) 661–680.
[4] S. Pradeep Narayanan, G. Venkatarathnam, Analysis of performance of heat exchanger used in practical micro miniature refrigerators, Cryogenics 39 (1999) 517–527.
[5] M. Chorowski, E. Bodio, M. Wilczek, Development and testing of a miniature Joule–Thomson refrigerator with sintered powder heat exchanger, Adv. Cryog. Eng. 39 (1994) 1475–1481.
[6] H.J. Holland, J.F. Burger, N. Boersma, H.J.M. ter Brake, H. Rogalla, Miniature 10–150 mw Linde–Hampson cooler with glass-tube heat exchanger operating with nitrogen, Cryogenics 38 (1998) 407–410.
[7] Y. Joo, K. Dieu, C.J. Kim, Fabrication of monolithic micro channels for IC chip cooling, IEEE (1995) 362–367.

[8] J.S. Bullers, A miniature self regulating rapid-cooling Joule–Thomson cryostat, Adv. Cryog. Eng. 16 (1971) 205–213.
[9] K. Hedegard, G. Walker, S. Zylstra, Temperature sensitive variable area flow regulator for Joule–Thomson nozzles, in: Proceedings of the 4th International Cryocooler Conference, US Government Printing Office, Washington, DC, USA, 1987, pp. 217–226.
[10] B.A. Sherman, S.H. Schwartz, Jet impingement boiling using a JT cryostat, Cryo. Heat Transfer, HTD 167 (1991) 11–17.
[11] F.C. Chou, S.M. Wu, C.F. Pai, Prediction of final temperature following Joule–Thomson expansion of nitrogen gas, Cryogenics 33 (1993) 857–862.
[12] B.Z. Maytal, Performance of ideal flow regulated Joule–Thomson cryocooler, Cryogenics 34 (1994) 723–726.
[13] F.C. Chou, S.B. Chien, J.B. Chen, Preliminary experimental and numerical study of transient characteristics for a Joule–Thomson cryocooler, Cryogenics 35 (1995) 311–316.
[14] S.B. Chien, L.T. Chen, F.C. Chou, A study on the transient characteristics of a self-regulating Joule–Thomson cryocooler, Cryogenics 36 (1996) 979–984.
[15] W.M. Kays, A.L. London, Compact Heat Exchangers, McGraw-Hill, New York, 1964.
[16] T.M. Flynn, in: Cryogenic Engineering, Marcel Dekker, New York, 1997, pp. 50–70.
[17] B.A. Younglove, Thermophysical properties of fluids. 1. Argon, ethylene, parahydrogen, nitrogen, nitrogen trifluoride, and oxygen, J. Phys. Chem. Ref. Data 11 (Suppl. 1) (1982).
[18] H.J.M. Hanley, R.D. McCarty, W.M. Haynes, The viscosity and thermal conductivity coefficients for dense gaseous and liquid argon, krypton, xenon, nitrogen and oxygen, J. Phys. Chem. Ref. Data 3 (4) (1974) 979–1014.
[19] S. Angus, B. Armstrong, International Thermodynamic Tables of the Fluid State Argon, Int. Union Pure Appl. Chem. (1971) 1–99.
[20] R.H. Perry, D.W. Green, J.O. Maloney, Perry's Chemical Engineers' Handbook, McGraw-Hill, New York, 1997, pp. 318–337.
[21] G.G. Haselden, Cryogenic Fundamentals, Academic Press, New York, 1971, pp. 237–243.
[22] W.M. Rohsennow, J.P. Hartnett, Y.I. Cho, Handbook of Heat Transfer, McGraw-Hill, New York, 1998, pp. 85–125.
[23] KryoTech Inc., 1999. http://www.kryotech.com/hot-chips.asp.